Snow Particle Motion in Process of Cornice Formation

Hongxiang Yu[1,2], Li Guang[1], Benjamin Walter[4], Jianping Huang[1], Ning Huang[2], and Michael Lehning[3,4]

[1]College of Atmospheric Science, Lanzhou University, Lanzhou, 730000, China
[2]College of Civil Engineering and Mechanics, Lanzhou University, Lanzhou, 730000, China
[3]College of Architecture Civil and Environmental Engineering, Ecole Polytechnique Federal de Lausanne, Lausanne, 1015, Switzerland
[4]WSL Institute for Snow and Avalanche Research SLF, Davos, 7260, Switzerland

Correspondence: Ning Huang (huangn@lzu.edu.cn) and Michael Lehning (lehning@slf.ch)

Abstract. Snow cornices are a common snow pattern in cold regions, and their fracture and collapse can easily trigger avalanches. Despite numerous observations and experimental simulations on their formation process, the microscopic mechanism of their initial stage of formation remains unclear. In this paper, based on wind-tunnel experiments and high-speed photography, experimental studies on the trajectory of particles surrounding the snow cornice were carried out. The experiment results reveal the distinct differences in particle size, impact velocity, and impact angle between the surface and edge of a cornice. The findings show that edge-deposited particles are generally smaller and more dendritic, attaching mainly through low-velocity saltation and mechanical interlocking, while surface deposition is dominated by larger, faster particles. The different probability distributions of impacting velocities and angles in these two regions are attributed to variations in airflow and local cornice topography. Both surface and edge regions, however, exhibit a characteristic vertical impact velocity threshold of 2–2.5 m/s, which is the dominant parameter governing particle adherence or rebound. A static adhesion model incorporating particle morphology parameters for edge deposition was developed and experimentally validated, confirming its effectiveness in predicting the influence of particle size, shape, and adhesion thresholds. Overall, this research reveals the micro-dynamics underlying initial cornice growth, providing a theoretical basis for avalanche modeling and infrastructure protection in alpine environments, as well as offering a methodological and mechanical framework for studying snow and ice adhesion in both natural and engineered systems.

NOTATION

Symbol	Definition and units
A	Weighting parameter for dendricity
A_p	Projected area of one particle [m^2]
D	Diameter of particle [m]
R_{th}	Threshold radius for particles adhering to the edge [m]
v_{p}	Particle velocity [m s^{-1}]
v_{px}	Particle velocity component in x direction [m s^{-1}]
v_{py}	Particle velocity component in y direction [m s^{-1}]
v_{imv}	Vertical impact velocity of particle [m s^{-1}]
F_c	Cohesive force [N]
F_f	Frictional force [N]
F_g	Gravity force [N]
F_s	Supporting force [N]
M_s	Total moment [N·m]
x	Radius of contact surface [m]
t	Current time [s]
τ_b	Bond shear stress [Pa]
Δt	Time step [s]
T_{air}	Air temperature [^{o}C]
θ_p	Particle moving angle [^{o}]
θ_{im}	Particle impact angle [^{o}]
θ	Cornice angle [^{o}]
α	Angle between direction of gravity and cohesion force [^{o}]
β	Angle between direction of gravity and line $\overline{OP}$ [^{o}]
μ_f	Friction coefficient of ice surface
ρ_i	Ice density [kg/m^3]
δ	Ratio of contact radius to particle radius
dd	Dendricity
SSA	Specific surface area [mm^2/mm^3]

1 Introduction

Snow consists of ice crystals. Snow particles may adhere to the surface at particle-bed collision. Therefore, wind can shape the snow cover and produce special patterns by redistributing snow over various areas, such as sastrugi, snow dunes (Sommer et al., 2018b), and snow cornices (Seligman et al., 1936). Snow cornice is one of the naturally formed accumulation patterns in cold mountain regions. Their collapse may induce snow avalanches (Vogel et al., 2012).

Previous field observations have consistently shown that the optimal wind speed range for cornice formation lies between one and two times the threshold wind speed (Vogel et al., 2012; Eckerstorfer et al., 2013; Hancock et al., 2020). Recently, wind-tunnel experiments have further shown that cornice growth is maximized when the wind speed exceeds the threshold value by 40% (Yu et al., 2022). However, the micro-mechanism for particle adhesion to the cornice edge has not been studied in detail, due to the difficulty in observing the formation process at the particle scale.

The growth of a snow cornice can be divided into several stages (Montagne, 1980; Vogel et al., 2012; Eckerstorfer et al., 2013). In the initial stage, a thin slab forms at the mountain edge (highlighted in red in Fig. 1), mainly by adhesion of wind-transported snow particles. When more snow accumulates on the relatively flat surface above the edge, it can gradually be conveyed toward the slab tip—especially via wind-transported particles—thereby increasing the thickness at the cornice root. This sustained supply of snow from the platform region plays a key role in the transformation of a small slab into a fully developed cornice in nature. In the subsequent stage, repeated deposition from intermittent drifting and precipitation successively adds new layers of snow to the cornice. This layer-by-layer accumulation is accompanied by a gradual increase in both length and thickness of the cornice. As the cornice grows larger, the overhanging mass of snow is increasingly influenced by gravitational forces, which may cause it to bend downward (shown in the white dashed line in Fig. 1) and promote internal compaction near the edge. Eventually, when the cornice becomes too large and shear stress exceeds a critical threshold, it breaks off and collapses. The evolution of a wedge-shaped cornice—from initial slab formation to subsequent snow accumulation on the flat surface—has been experimentally investigated in our previous work (Yu et al., 2022), with particular focus on the relationship between cornice growth rate and air mass transport. However, the specific mechanisms governing the very initial stage, that is, how airborne snow particles first adhere and accumulate to form the small slab at the edge, remain unexplored.

Previous field research mainly focused on the morphology variation due to limitations of observation equipment (Vogel et al., 2012; Eckerstorfer et al., 2013; van Herwijnen and Fierz, 2014; Hancock et al., 2020), for observing how particles adhering to mountain edges are hardly realized. Currently, there are several hypotheses on how snow particles adhere at the edge: Irregularly-shaped snow particles interlock with each other by their dendrites (Seligman et al., 1936); Charged snow particles are attracted by the strong electric field above the snow cornice surface (Latham and Montagne, 1970); Pressure melt and frictional heat (Latham and Montagne, 1970) when particles contact other

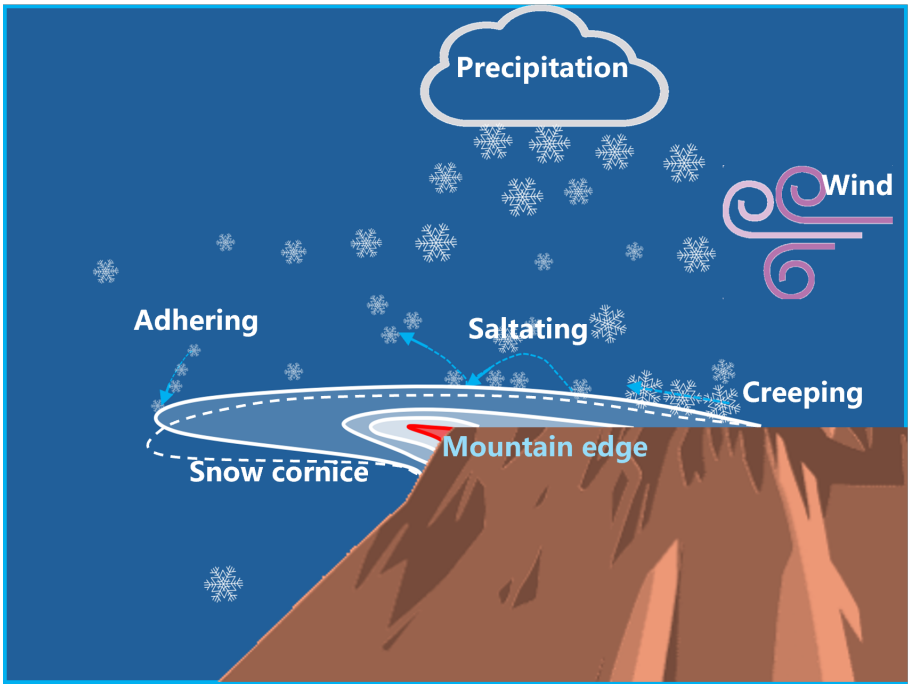

Figure 1. Schematic diagram of different stages in snow cornice growth.

surfaces leads to a quasi-liquid layer facilitating fast sintering. However, the mechanism behind the wedge-shaped (Seligman et al., 1936) snow cornice has not yet been investigated.

Cornice growth is often accompanied by drifting snow (Eckerstorfer et al., 2013; Yu et al., 2022), in which a snow particle saltation layer exists. Drifting snow particles move in three modes, namely, creep, saltation, and suspension, with the first two modes contributing most to snow mass transport (Bagnold, 2012). When snow particles collide with the surface, three processes may occur: 1) Rebound occurs when a portion of particle kinematic energy is lost, but may rebound from the surface; 2) Deposition occurs when the particle loses all its kinematic energy upon impact with the ground; 3) Eject occurs when the particle transfers the kinematic energy to other particles on the ground upon impact with surface, resulting in the entrainment of other particles resting on the surface.

During particle-surface collision, the particles transfer momentum and energy from the air to the surface. These processes are characterized using rebound and splash functions based on theoretical models (Lämmel et al., 2017; Comola and Lehning, 2017) or observations (Anderson and Haff, 1991). Particle impact velocity and impact angle (Walter et al., 2023) are two critical factors influencing key processes such as rebounding, deposition, and splashing. These parameters play a significant role in determining how particles interact with surfaces upon collision. However, the specific method by which particle impact velocity and impact angle influence particle adhesion, particularly in the context of snow cornice formation, remains poorly understood. Thus, investigation is needed to clarify the relationship between these impact parameters and the adhesion mechanisms.

Here, we carry out a wind-tunnel experiment of cornice formation, focusing on particle trajectory and adhesion process in snow cornice formation. Based on the experimental results, we investigate the micro-physical mechanism for cornice formation.

2 Instruments and methods

The wind-tunnel experiments are carried out in a ring wind tunnel in the cold lab of the WSL Institute for Snow and Avalanche Research, in Davos, Switzerland. The experiment setup is shown in Fig. 2. The working section of the wind tunnel is 1 m in length, with a cross-section area of 0.2 m (width) × 0.5 m (height), and has been successfully used for several drifting snow experiments (Wahl et al., 2024; Walter et al., 2024; Yu et al., 2022; Sommer et al., 2017, 2018a). Further details of the wind tunnel can be found in Yu et al. (2022). For tracing particle trajectories, a high-speed camera system is deployed. A feeding system is used to supply snow particles. The feeding rate of snow particles is manually kept stable. The snow particles are produced by a snow maker (Schleef et al., 2014). The geometrical diameters are 300–500 μm, and the shape of the snow crystals is dendritic, visually analyzed under a microscope. The room temperature of the cold lab is controlled and set at =5 °C, and the wind speed is kept at 4 m s^{-1}. The wind speed inside the wind tunnel is nearly uniform with a very thin (around 2 cm) boundary layer (Sommer et al., 2017; Yu et al., 2022). A ridge model with a fixed size (Fig. 2) is built with compacted snow before each experiment. A ridge model with a fixed size (height 0.125 m, total length 0.4 m, flat surface length 0.1 m) is built with compacted snow before each experiment, and its side view is shown in Fig. 2.

Before conducting the experiment, we performed preliminary tests on both fresh snow particles and aged snow particles. Fresh snow particles, characterized by their highly dendritic shapes, were compared to decomposed snow particles, which are characterized by small, rounded shapes after being stored for several days at a constant temperature of $T_{air} = -10^o$C. The results show that both types of snow particles are capable of forming a snow cornice. However, fresh snow particles exhibit a significantly higher propensity for cornice formation and are much easier to consolidate into a stable structure. Therefore, fresh snow particles were used in the subsequent experiments.

The high-speed camera system consists of a high-speed camera (Phantom VEO710), an LED lamp as a light source, and a transparent plane positioned at the opposite side of the camera to diffuse the light source and achieve uniform illumination. The system is employed for shadowgraphy analysis. The shadowgraphy is a technique used for extracting the moving particle's size, velocity, and trajectory. It is similar to PTV (particle tracking velocimetry)(Baek and Lee, 1996; Tagliavini et al., 2022), which has the same algorithms for particle information, and it has been frequently used in recent snow-related studies, for its advantages in robustness, non-intrusiveness, and accessibility. Shadowgraphy is particularly suitable for tracking snow particles, which are partially transparent and irregular in shape. It has been successfully applied to measuring particle mass flux, velocity, and size distribution (Paterna et al., 2016; Walter et al., 2023). The sampling frequency of the camera is set as 3 kHz, corresponding to a time interval of 333.32 µs. A total of 18 cases were conducted during the cornice growth, with each case lasting 4—5 seconds and yielding

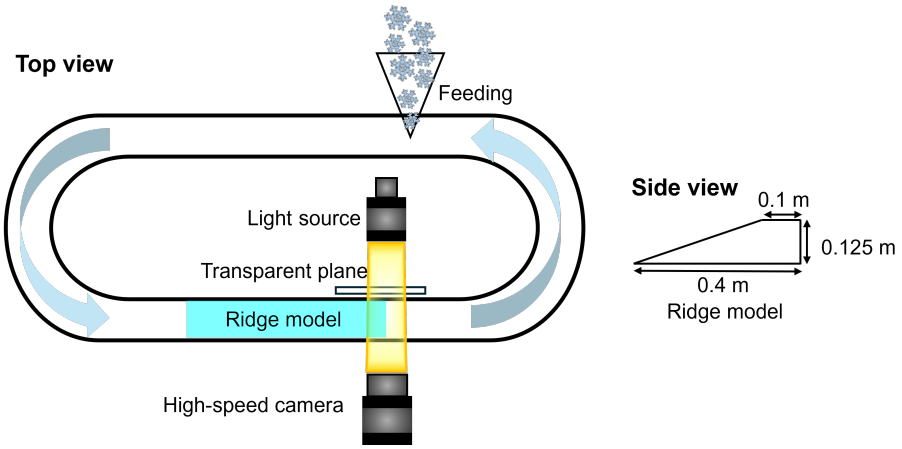

Figure 2. Schematic for experimental setups.

12455 images to record the particle trajectories. The duration of each case was limited by the camera memory. A sequence of the different growth steps is illustrated in Fig. 3(a) of Yu et al. (2022). After the images are obtained, particle-bed collision events are selected visually. Then, particle sizes and trajectories in these events are analysed by image processing as follows.

2.1 Particle recognition

The gray value of the snow cornice base is much higher than that of airborne snow particles. Thus, the images are first transferred into binary format by the two threshold gray values to recognize both the snow cornice base and airborne snow particles. The cornice zone is detected according to the first threshold gray value. The airborne snow particles are then detected according to the second threshold gray value after extracting the cornice from the image.

Particle size as recognized by the first-time binary analysis using the second threshold gray value is normally smaller than its real size, as shown in Fig. 3(a)-(b). To compensate for the underestimated particle areas caused by binarization, a dilation process (Gonzalez and Woods, 2017) is applied after the binarization, which fills the small spaces around the snow particle and smooths the particle's boundary, as depicted in Fig. 3(c) and its zoomed-in counterpart in (d).

To distinguish the noise points from air-flow snow particles, opening and closing processes (Solomon and Breckon, 2011) are then operated. The opening process eliminates very fine objects (noise points) and smooths the snow cornice boundary, and the closing process corrects the image such as filling the tiny empty holes inside of the snow particles.

After the above image pre-processing, particle recognition is carried out by using the Seed-Filling Algorithm (SFA). SFA is an algorithm used to fill closed regions in an image. It starts from a seed point and gradually fills the regions adjacent to it with the same color until the boundary is reached. Snow particle area is calculated based on

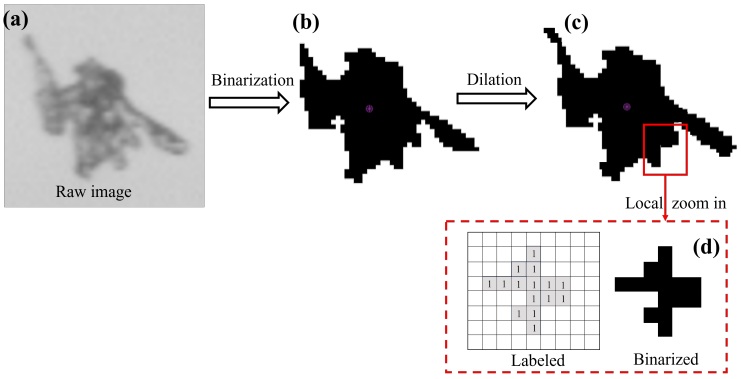

Figure 3. Image pre-processing method

the connected component label analysis (CCLA), a common image processing method for connecting the adjacent foreground pixels that have the same pixel value (Di Stefano and Bulgarelli, 1999; Rafael and Richard, 1993).

During image processing, the particle's area and perimeter are saved in a numerical matrix in binarized format. Thus, the particle's projected area A_p can be estimated by calculating the sum of all the connected component labels, and the particle's perimeter P is the sum of all the boundary labels. The particle's equivalent diameter is calculated based on the value of its projected area: $d_e = \sqrt{4A_p/\pi}$. The dendricity of each particle was quantified using the method proposed by (Bartlett et al., 2008), based on two-dimensional image analysis. Specifically, dendricity was calculated as $dd = \frac{P^2}{4\pi A_p}$. The specific surface area (SSA) of particles was estimated from two-dimensional images by measuring the perimeters and areas of particles, following the stereological approach proposed by (Ren et al., 2021). According to this method, SSA is calculated as $SSA = \frac{4\overline{P_i}}{\pi \overline{A_i}}$. This approach enables the statistical analysis of SSA distribution based on 2D image data, and its validity and limitations have been demonstrated in comparison with three-dimensional and conventional measurement methods. For dendritic particles, the projected area A_p and perimeter P were averaged across these frames for each particle, which effectively minimizes the influence of particle orientation on the calculated size. All pre-processing of images (dilation, opening, closing operations) and particle recognition in this work are programmed using the MATLAB software.

2.2 Particle trajectory tracking

By using the above particle recognition method, we obtained a series of images that contain the particle information. Then, the trajectory and velocity of snow particles are obtained using the trajectory recognition method that judges the relative position of the neighboring particles.

We paired each particle from the previous time series of images by using the nearest-neighbor algorithms (NNA) (Crocker and Grier, 1996) to match the targeted particle's position in each frame image. NNA is a particle search method, as shown in Fig. 4. In each time step, we search for the position of the target particle in the last frame of

an image within the predefined search radius. The center of the corresponding circle area is assumed to be at the mass center of the target particle in the last frame, and the radius is 6 mm. We then match the target particle by its shadow surface area similarity. By recognizing the position of the target particle in each frame image, we obtain the velocity of the target particles.

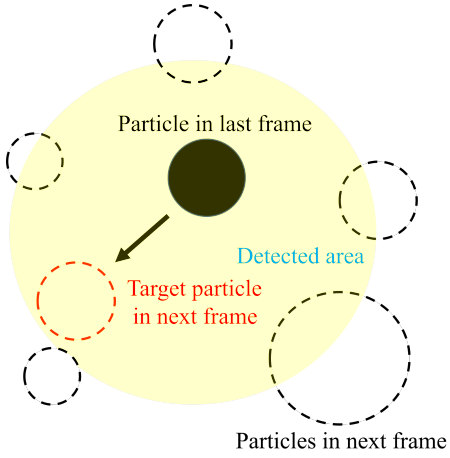

Figure 4. Schematic of particle detection method in post-processing high-speed camera images. The full circle is the particle from the last frame, the dashed circle is the particles from the second frame, and the yellow region is the predefined search area.

The k_{th} target particle's horizontal and vertical velocity at a given time step Δt is calculated as:

$$v_{px}(t) = \frac{x(t+\Delta t) - x(t)}{\Delta t} \tag{1}$$

$$v_{py}(t) = \frac{y(t+\Delta t) - y(t)}{\Delta t} \tag{2}$$

in which x and y are the coordinate positions in x-axis and y-axis, t is the current time, and Δt is the time interval of a high-speed camera. Therefore, the magnitude of particle velocity v_p is:

$$v_p(t) = \sqrt{(v_{px}(t))^2 + (v_{py}(t))^2} \tag{3}$$

where v_{px} and v_{py} are the velocity component in x and y direction, respectively. The particle moving angle θ_p can be calculated as:

$$\theta_p(t) = \arctan(\frac{|v_{py}(t)|}{|v_{px}(t)|}) \tag{4}$$

A particle contact event is defined when the particle's vertical velocity is from negative (downward) to zero or positive (upward) among several adjacent images. The impact velocity is then defined as the velocity before the contact, and the rebound velocity is defined as the velocity after the contact. We found the maximum error between visual observation (manually tracking the particle's trajectory) and program recognition of the edge particle velocity to be 5%, the angle to be 18%, and the diameter to be 16%.

3 Results and discussions

By maintaining the wind speed in the experiment at a constant (4 m/s), the study analyzed 655 collision particles interacting with the snow surface. These interactions included particles that rebounded, impacted, or deposited on the snow, as determined through an image post-processing method. Among these particles, 186 adhered to the cornice edge, while 469 adhered to the cornice upper surface. The cornice edge here refers to the spatial range of the 1 mm vertical front end of a dynamically growing cornice, and the cornice surface refers to the cornice's topside with the total length at the current time step minus the edge length, as is shown in Fig. 5(a).

The distributions of the snow particle impact velocity, impact angle, and size distribution are shown in Fig. 5(b). The blue points represent the particles that adhere to the edge and the red points represent those that adhere to the surface. The size of all points represents the particle's diameter. It can be concluded that particles that adhere to the edge have relatively lower and more narrowly-distributed values of impact velocity, but widely-distributed impact angle, compared to the particles that adhere to the surface.

To investigate the differences between edge and surface particles, we analyzed the adhere particle's size distribution, impact velocity, and impact angle in the following sections.

3.1 Particle size and shape

The size distribution of particles adhering at different positions on a dynamically evolving cornice is analyzed, as shown in Fig. 6. For all particles adhering to the cornice surface, their size distribution follows the Log-normal distribution described by $\theta \sim N(\mu$=277.17, θ=0.45), with the average diameter $\overline{D}_{all} = 340$ um. For particles adhering at the edge, their size distribution follows the Log-normal distribution described by $\theta \sim N(\mu$=264.42, θ=0.38), with the average diameter $\overline{D}_{edge} = 329$ um. For particles adhering to the surface, their size distribution follows the Log-normal distribution function described by $\theta \sim N(\mu = 342.69$, θ=0.28), with the average diameter $\overline{D}_{surface}$=405 um. It can be concluded that particles with smaller sizes adhere more likely on the edge, and larger particles adhere more likely on the cornice surface.

In addition to particle size, dendricity and specific surface area (SSA) are important indicators of particle morphology and surface characteristics. As illustrated in Fig. 7(a), the average dendricity of edge particles is 1.9, higher than that of surface 1.4. Meanwhile, the distribution range of the edge particles (1 to 4.7) is broader than that of

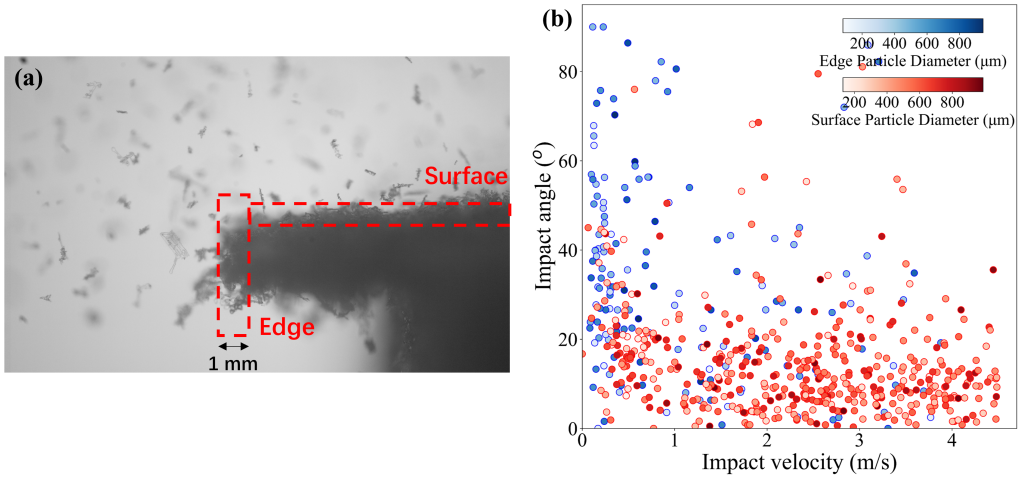

Figure 5. (a) Cornice edge and surface, with the dashed box indicating the regions of edge and surface. (b) Impact velocity and impact angle of snow particles of different sizes (deeper color represents larger size) on edge (in blue points) and surface (in red points).

the surface particles (1 to 3.1). These results indicate that the edge particles have more fragmented or branched morphologies, while particles on the surface are generally more regular and compact.

However, the SSA values of edge particles and surface particles are similar, with the average value of $20\ \mathrm{mm}^2/\mathrm{mm}^3$, as is shown in Fig. 7(b). This similarity arises because both edge and surface particles originate from the same snow source. Therefore, dendricity is a more critical factor in determining whether a particle can adhere to an edge or the surface. In particular, edge particles with high dendricity have more contact points with neighboring particles on the cornice, which may lead to a greater cohesion force F_c—the force counteracts the gravity force F_g and allows the edge particle to adhere. In contrast, surface particles may experience less cohesion force, and their gravity acts in the same direction as the cohesion force, making gravity either irrelevant or even beneficial for particle adherence.

Combining the analysis of particle size, dendricity, and SSA distribution, we find that smaller particles and dendritic particles are more prone to adhere to the edge, while larger and more spherical particles tend to deposit on the surface. This phenomenon is closely related to the aerodynamic behavior of particles in the air. Specifically, the pattern of particle deposition is primarily governed by the Stokes number (Comola et al., 2019), a dimensionless parameter that compares the inertial response time (particle relaxation time) of a particle to the characteristic time scale of the fluid flow. In general, particles with smaller sizes, as well as large particles with irregular shapes, tend to have lower relaxation times than spherical particles of the same size (Loth, 2008). As a result, for such small particles and large, highly dendritic ones, viscous forces dominate over inertia, enabling the particles to quickly respond to changes in local fluid velocity and closely follow the streamlines. Such particles therefore preferentially deposit on the edges—where the wind speed is near zero and accompanied by a reflux vortex (DeBonis, 2022). In

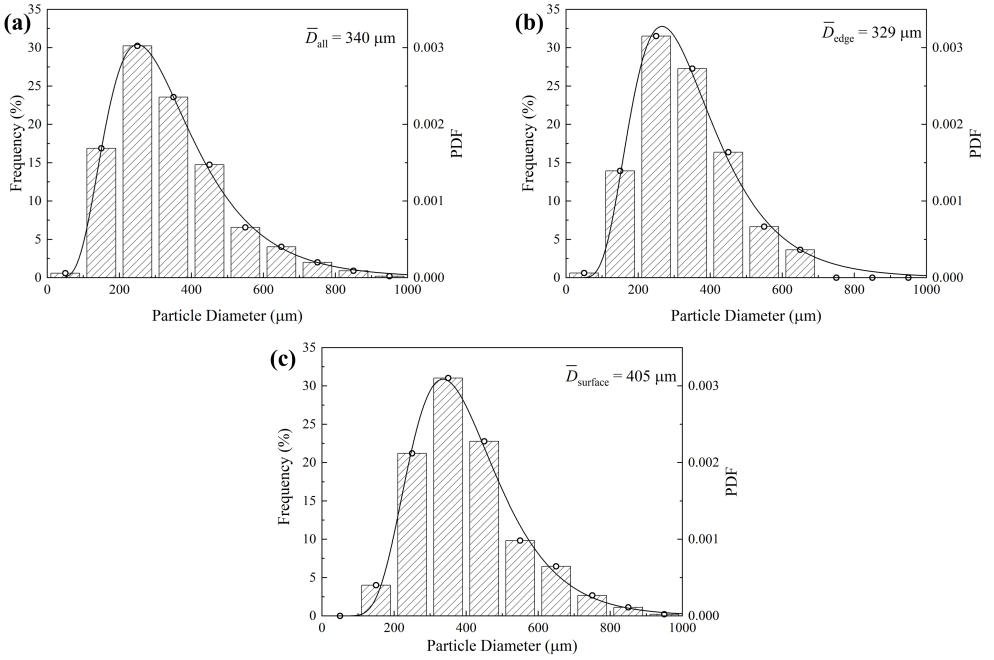

Figure 6. Size distribution of particles at different positions. (a) Airborne particles. (b) Adhesion particles at the edge. (c) Adhesion particles on the surface. The gray shadow represents the existence frequency of particles with different sizes.

contrast, for spherical particles, especially those with larger size, inertial forces become more significant relative to viscous drag, making these particles less responsive to fluid velocity changes and more likely to deposit on the main surfaces—which are generally characterized by a stable boundary layer and low turbulence.

3.2 Particle movement pattern

Near-surface moving particles were captured by using a high-speed camera. Creeping (particles rolling or sliding over the surface before retaining) and saltating (particles successively jumping over the surface before settling) (Bagnold, 2012) are the two primary modes contributing to cornice growth. Creeping particles (Fig. 8(a)), which account for about 14% of the observed particles, represent the minority of larger-sized adhered particles, and they typically move slowly. These particles are mainly entrained from the surface under the ejection of other particles. Most of them retain on the cornice surface, and only a small fraction—with elongated dendrites—are able to interlock and remain adhered at the edge (Fig. 8(b)).

In addition, saltating particles observed near the cornice originate either from airborne trajectories or from ejection off the surface. Whether saltating particles rebound or deposit on the cornice surface after impact is strongly influenced by their impact position, velocity, and angle. Among all the particles that settle on the cornice surface,

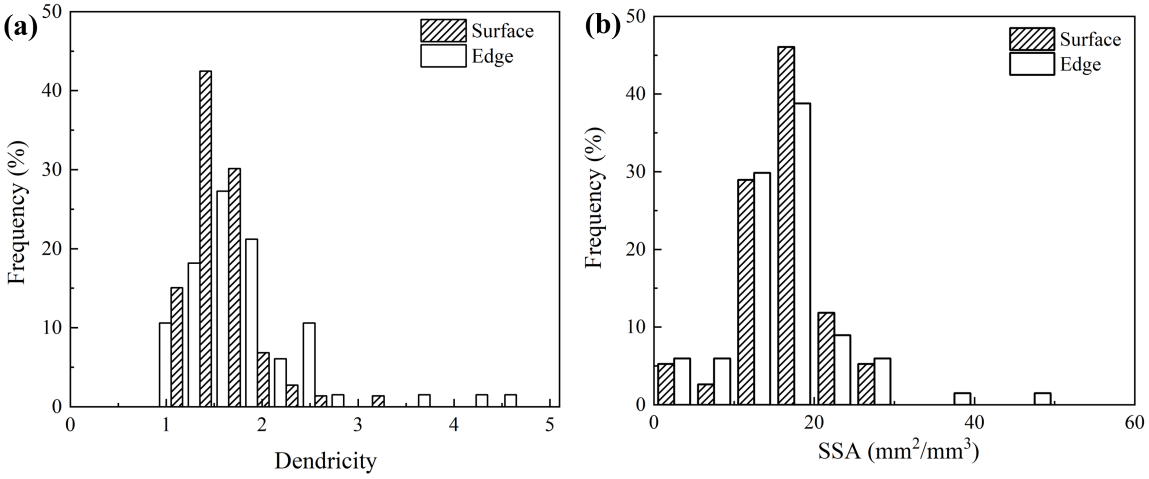

Figure 7. Frequency distributions of (a) dendricity and (b) specific surface area (SSA) for particles adhering to the edge and surface.

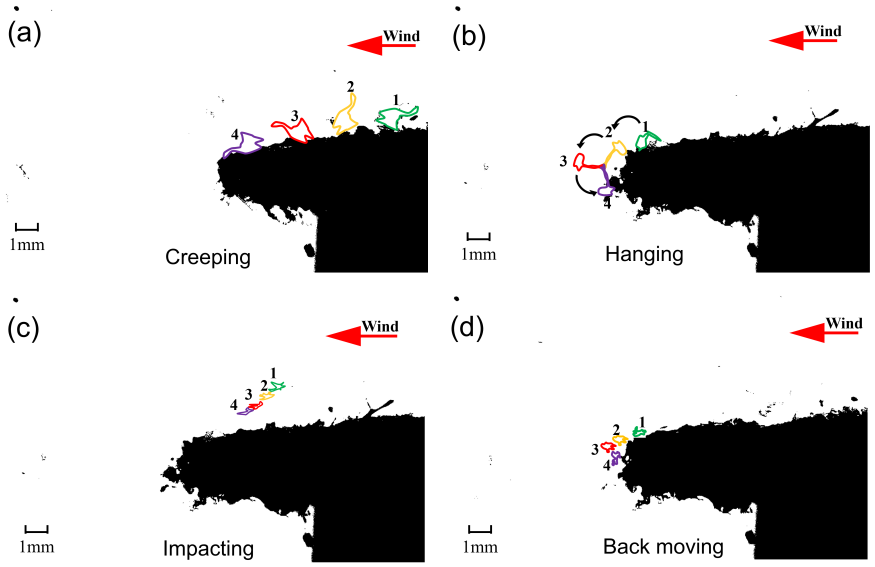

Figure 8. Four adhering patterns of snow particles (1,2,3,4 represents for different time steps).(a) Creeping particles. (b) Hanging particles. (c) Impacting particles. (d) Back moving particles.

about 82% are saltating particles that deposit before reaching the cornice's front end, as is shown in Fig. 8(c). Only an extremely small number of particles deposit on the front end, which are smaller-sized particles ejected near the

edge. Fewer saltating particles going off the edge will later move backward to the cornice edge, under the action of the reflux vortex or the potential electric field, as shown in Fig. 8(d).

3.3 Particle impact velocity and angle

Here, we define the v_{im} as the impact velocity of the particle θ_{im} is defined as the angle of particle incidence on the horizontal cornice surface, ranging from 0^o (parallel to the surface) to 90^o (perpendicular to the surface), and this angle measures how steeply a particle approaches the surface or edge before sticking. Only particles impacting the cornice surface from above (incidence angle 0—90^o) are considered, while particles with trajectories suggesting backward-moving ($\theta_{im} > 90^o$) are excluded. We first analyze the v_{im} and θ_{im} of 469 particles adhered on the surface and 186 particles adhered on the edge. In natural conditions, the snow cornice will slowly bend and deform under the gravity force. In our experiment, the snow cornice can be considered as horizontally growing in the whole process, and the bending effect of the snow cornice can be neglected for the short observation time. We subdivided the values of v_{im} and θ_{im} into different bins and analyzed their relative frequency. The average value of each bin is plotted as dots and the standard deviation is plotted as error bars in Fig. 9.

The relative frequencies of v_{im} and θ_{im} represent the probabilities of particle adhesion on the cornice with a certain impact velocity or impact angle. It is shown in Fig. 9(a) that for edge particles, the adhesion probability exponentially decreases with the increasing value of v_{im}. Specifically, the relative frequency of v_{im} of edge particles follows the exponential function $f(v_{im}) = 4.3 + 30e^{-0.9v_{im}}$ ($R^2 = 0.96$). This indicates that particles with lower impact velocities are more likely to adhere to the edge. The majority of edge particle adhesion occurs at velocities below 1.5 m/s, highlighting the critical role of low-velocity impacts in cornice growth. While the relative frequency of v_{im} of surface particles follows the the Gaussian distribution function of $f(v_{im}) = -2.8 + \frac{79}{3.4\sqrt{\pi/2}} e^{-2(\frac{v_{imp}-2.9}{3.4})^2}$ ($R^2 = 0.91$), with values mainly concentrated at 3 m/s. This indicates that particles deposited on the surface normally have a higher impact velocity than the edge. This is because the snowpack on the surface is thicker than at the edge, as the cornice has a wedge shape. As a result, the surface can absorb more impact energy through longer force chains, allowing particles with higher impact velocities to adhere. In contrast, the thinner snowpack at the edge cannot effectively dissipate kinetic energy, so high-speed particle impacts often lead to erosion or fracture at the edge.

The low number of particles adhering to the surface at low impact velocities can be attributed to the wind speed in the wind tunnel, which is set at 4 m/s. At this wind speed, the majority of particles are entrained and transported at higher velocities, leaving only a small fraction of particles moving at very low velocities near the cornice's surface.

As is shown in Fig. 9(b) that the frequency of θ_{im} of surface particles follows the Exponential distribution function $f(\theta_{im}) = -0.8 + 80.6e^{-0.1v_{imp}}$ ($R^2 = 0.97$), with values mainly concentrated below 17°. While the frequency of θ_{im} of edge particles follows the Gaussian distribution function $f(\theta_{im}) = 7.1 + \frac{448.8}{45.7\sqrt{\pi/2}} e^{-2((v_{imp}-18.1)/45.7)^2}$ ($R^2 = 0.72$), with values distributed more uniformly in range. The average value of θ_{im} of surface particles is 13°, which is consistent with the previous experimental results of Nishimura and Hunt (2000), as is shown in the red dash in Fig. 9(b). Particles at the edge can adhere even at higher impact angles, as the edge provides a partially sheltered

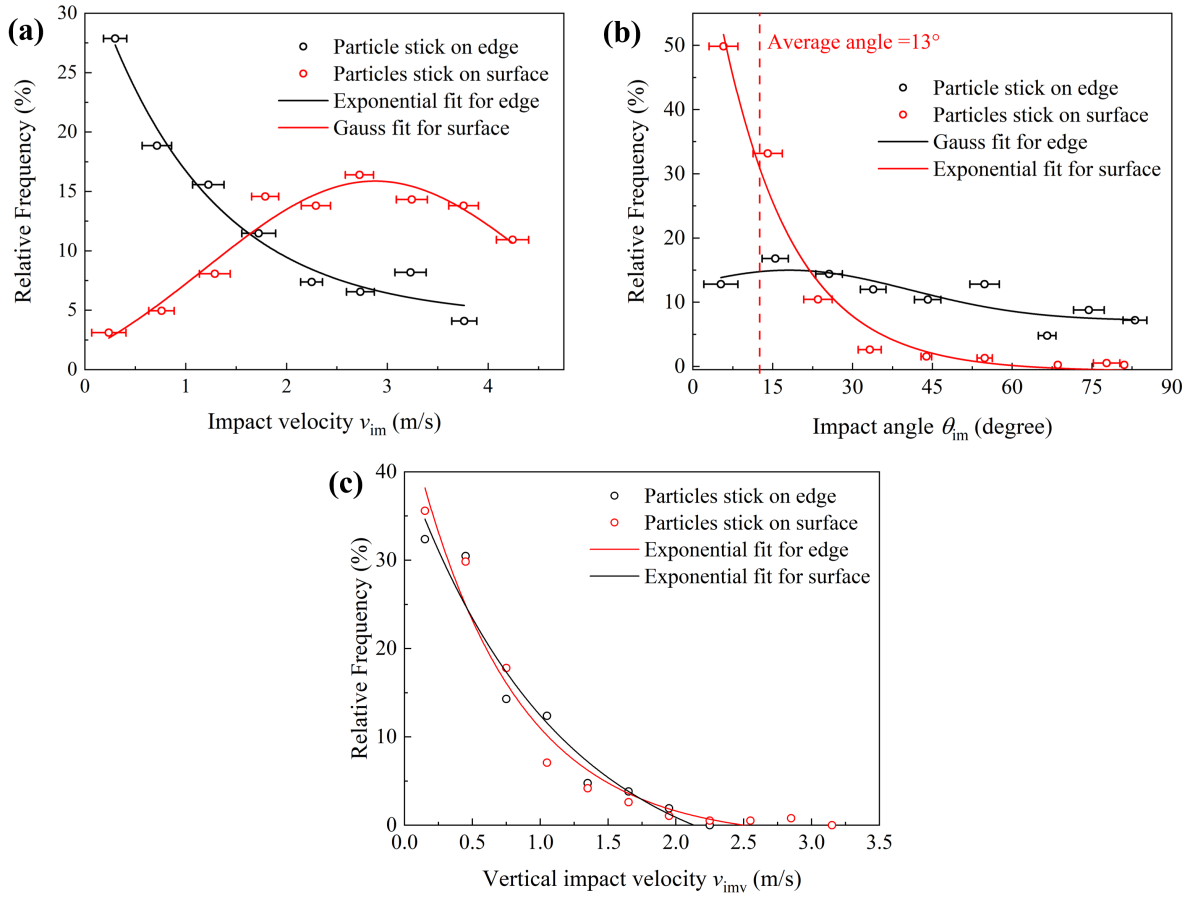

Figure 9. Relative frequencies of (a) impact velocity, (b) impact angle, and (c) vertical impact velocity of particles adhering to the edge and surface.

micro-environment where the local wind speed is lower. This reduction in wind velocity decreases the tendency for particle rebound and thereby increases the likelihood of adherence, even under conditions of increased impact angle.

Furthermore, we combined the impact velocity and angle by analyzing the vertical impact velocity ($v_{imv} = v_{im}sin\theta_{im}$) in Fig. 9(c). The relative frequency of v_{imv} for both surface particles and edge particles follow the exponential distribution, with surface particles $f(v_{imv}) = 0.5e^{-v_{imv}/0.7}(R^2 = 0.96)$, and edge particles $f(v_{imv}) = -0.1 + 0.5e^{-0.9v_{imv}}(R^2 = 0.95)$. Particles adhere at low vertical impact velocities, whether on edges or surfaces. For both edge and surface particles, the threshold vertical impact velocity ranges from 2-2.5 m/s, with edge particles having a lower threshold velocity compared to surface particles. The differences in impact velocity and angle distributions between surface and edge are due to the fluid field differences caused by topographic changes. It is noted that the vertical impact velocity distributions of surface particles and edge particles are in the same trend, although

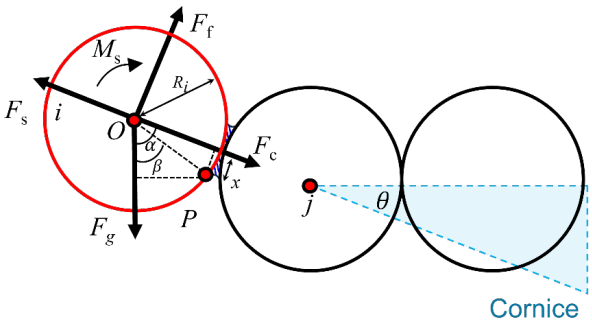

Figure 10. Schematic diagram of force analysis of particles adhering to the edge.

the impact velocity and impact angle distributions of edge particles and surface particles are different. It indicates that particle adhesion can be affected by the vertical impact velocity. This is because only the vertical kinetic energy provided by the normal velocity can be used to overcome the adhesion energy barrier of the surface, whereas the tangential velocity cannot assist the particle in detaching from the surface in the vertical direction (John, 1995).

3.4 Static force analysis of adhering particles on the cornice edge

To investigate the effect of dendricity on the article adherence at the edge, forces acting on a particle adhering to the edge are analyzed in this section.

Considering the differences in particle size distribution between the edge particles and surface particles, we conducted a static analysis of the particles at the edge. As shown in Fig. 10, a newly deposited particle i adheres to the foremost particle j at the edge of the cornice. Particle i is subjected to gravity F_g, the cohesive force F_c exerted by particle j, and the frictional force F_f at the contact surface. Due to the separation of flow, the wind velocity and surface shear stress near the edge of the cornice are close to zero (DeBonis, 2022; Shehadi, 2018), allowing the drag and lift forces acting on particle i to be neglected compared to other forces (Schmidt, 1980).

The force balance equations for particle i can be expressed as:

$$F_g \cos\alpha + F_c = F_s \tag{5}$$

$$F_g \sin\alpha \leq F_f \tag{6}$$

$$F_f = \mu_f F_s \tag{7}$$

Here, F_g is the gravity force on particle i, F_c is the cohesive bond force, given by $\pi x^2 \sigma$ (Szabo and Schneebeli, 2007), where σ is the tensile strength at failure and x is the radius of the bond (blue shadowed area). F_s is the supporting force, and α is the angle between the direction of gravity and cohesive force. R_i is the radius of particle i.

When snow particles adhere to the surface, both the gravity force F_g and the adhesive force F_c are in the vertical direction, resulting in an upward support force from the surface that maintains their stationary position. However, when snow particles adhere to the edge, the gravity force F_g and the adhesive force F_c are not in the same direction. The component of the cohesive force in the direction of the gravity force is balanced by the support force generated by the edge, while the component of the gravity force perpendicular to the adhesive force needs to be balanced by friction force F_f. Once this component exceeds the frictional force, the particles will fall.

By substituting Eq. (5) and Eq. (7) into Eq. (6), we can derive the condition for particle i to maintain mechanical equilibrium if:

$$\frac{F_c}{F_g} \geq \frac{\sin\alpha}{\mu_f} - \cos\alpha \tag{8}$$

To analyze the stability of particle i, overturning moments are calculated around point P (at the edge of the bond). The supporting force F_s and cohesive force F_c act through the center of particle i and operate on point P through the moment arm x. The gravity force F_g acts on point P through the moment arm $Rsin(\alpha - arcsin(x/R))$, where the angle between F_g and line $\overline{OP}$ (distance from particle center to point P) is $\beta = \alpha - arcsin(x/R)$. The friction force F_f acts on point P through the moment arm $Rcos(arcsin(x/R))$. The condition for the particle to remain in equilibrium is when the total moment $M_s = 0$. Therefore:

$$(F_s - F_c)x + F_g R sin(\alpha - arcsin(\frac{x}{R})) - F_f R cos(arcsin(\frac{x}{R})) = 0 \tag{9}$$

Substituting Eq. (5) and Eq. (7) into Eq. (9) yields:

$$\frac{F_c}{F_g} = \frac{x/R \cdot cos\alpha + sin(\alpha - arcsin(x/R)) - \mu_f cos\alpha cos(arcsin(x/R))}{\mu_f cos(arcsin(x/R))} \tag{10}$$

In which F_c is the cohesion force, which can be expressed as:

$$F_c = \pi x^2 \tau_b \tag{11}$$

where x is the contact radius of ice bridge, assumed here to vary linearly with particle radius $x = \delta R$, with ratio δ = 0.1—0.25 (Golubev and Frolov, 2001). τ_b is the bond shear stress. While for non-spherical particles, particularly those with dendritic structures, the cohesion force is higher than that of spherical particles, due to the stronger geometrical interlocking between particles. Thus, dendricity should be considered in the calculation of the cohesion force for non-spherical particles. Here, we introduce a weighting parameter A into the cohesion force equation for dendritic particles, and its value will be derived later.

$$F_c = \pi x^2 \tau_b (1 + A(dd - 1)) \tag{12}$$

where dd is the dendricity value of non-spherical particles. For spherical particles, dendricity is a constant: dd =1, and cohesive force is only determined by contact radius, $F_c = \pi x^2 \tau_b$. For those particles that adhere on the edge, the average value of dendricity dd= 1.9, as is shown in Fig. 7.

The gravitational force of the particle is:

$$F_g = 4/3\pi R^3 \rho_i g \tag{13}$$

By substituting Eq. (12) and (13) into the left side of Eq. (10), we obtained the expression for the ratio of F_c/F_g:

$$\frac{F_c}{F_g} = \frac{\pi x^2 \tau_b (1 + A(dd-1))}{4/3\pi R^3 \rho_i g} \tag{14}$$

Meanwhile, the right side of Eq. (10) can be defined as a function ϕ, which is affected by the ratio δ, angle α, and friction coefficient μ_f:

$$\phi = \delta cos\alpha + sin(\alpha - arcsin(\delta)) - \mu_f cos\alpha cos(arcsin(\delta))\mu_f cos(arcsin(\delta)) \tag{15}$$

In which, the friction coefficient μ_f ranges from 0.2 to 0.7 (McClung and Schaerer, 2006), and the angle α varies from 0 to 90^o according to the experiment result. The resulting values of ϕ are illustrated in the contour plot shown in Fig. 11. Notably, ϕ decreases with increasing μ_f at all α, which indicates that higher friction reduces the need for a strong cohesive force to maintain stability. For a given μ_f, ϕ increases at larger angles, meaning that higher cohesion is required to keep the particle stable at the edge. When angle $\alpha = 90^o$, the cohesion force is perpendicular to the gravity force; under this condition, the particle is most difficult to adhere to the edge. The bottom-right blank areas correspond to the instability status for particles where adhesion doesn't happen.

Considering the most challenging condition for a particle to adhere to the edge occurs when the angle $\alpha = s90^o$ and the friction coefficient $\mu_f = 0.2$. The corresponding $\phi \approx 5$. Therefore, by combining Eq. (10), (14) and (15), we can obtain:

$$\frac{F_c}{F_g} = \frac{\pi x^2 \tau_b (1 + A(dd-1)}{4/3\pi R^3 \rho_i g} = 5 \tag{16}$$

Based on the experimental results shown in Fig. 6(b), the maximum radius of particles adhering to the edge is 325 um. Therefore, we have:

$$\frac{4\delta^2 \tau_b (1 + A(dd-1))}{15\rho_i g} = 325 \times 10^{-6} \tag{17}$$

with $\delta = 0.1$, $\tau_b = 1$ kPa (Jamieson and Johnston, 1990), $dd = 1.9$, and $\phi_{max} = 5$, we can derive the value of parameter A ≈ 0.07.

Therefore, in general, the cohesion force for edge particles, considering the shape effect, can be expressed as:

$$F_c = \pi x^2 \tau_b (1 + 0.07(dd-1)) \tag{18}$$

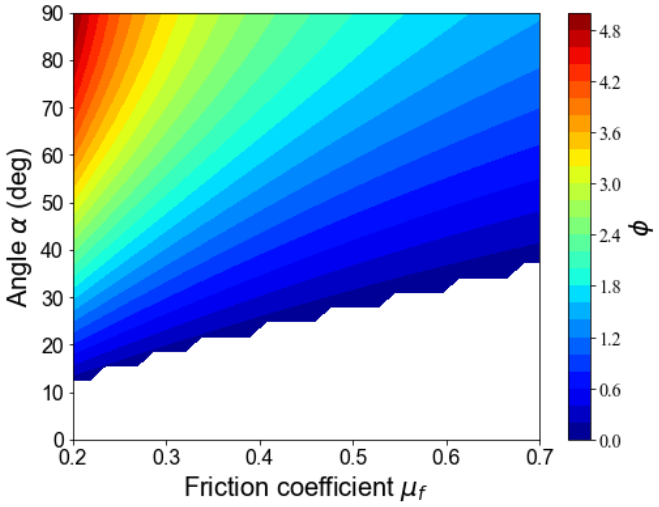

Figure 11. Variation of ϕ as a function of friction coefficient μ_f and angle α.

and the threshold radius R_{th} for particles that can adhere to the edge can be estimated by:

$$R_{th} = \frac{4\delta^2 \tau_b (1 + 0.07(dd - 1))}{3\rho_i g \phi_{max}} \tag{19}$$

The threshold radius R_{th} linearly increases with the increasing dendricity, in different δ values, as is shown in Fig. 12. With the higher value of ratio δ, it means a larger contact surface, therefore it allows larger particles adhering to the edge. δ is mainly dependent on the air temperature and relative humidity (Colbeck, 1982). Furthermore, we divided the radius into different bins based on the dendricity values. By comparing the averaged radius of various dendricity, we found that the experimental result is in good agreement with the model-predicted results. The experimental data lie between the theoretical curves for δ=0.15 and δ=0.25. It can be concluded that the maximum particle size capable of adhering to the edge increases with increasing dendricity. Which means greater dendricity enables larger particles to remain attached, suggesting that the complexity of the particle shape helps counteract gravity.

4 Conclusions

This study elucidates the micro-mechanisms underlying the initial formation of snow cornices through wind-tunnel experiments and high-speed particle tracking, facilitated by a novel snow particle recognition program. Direct observation and quantitative analysis reveal that near-surface saltation and creeping are the dominant mechanisms by which snow particles adhere to cornice structures. The vast majority of adhered particles settle on the upper surface via saltation, while only a smaller proportion is able to deposit or interlock at the front edge, often aided by their dendritic morphology.

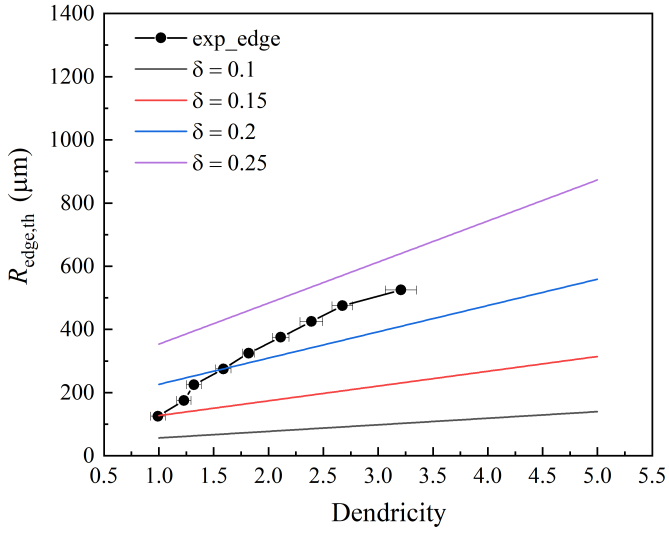

Figure 12. Experimental and theoretical threshold radius of edge-adhering particles as a function of dendricity for various δ values.

Our experiments demonstrate that, despite local variations in particle size, velocity, and impact angle, the adhesion of snow particles—on both edge and surface—is governed primarily by the vertical impact velocity, with an adhesion threshold between 2—-2.5 m/s. Edge-adhering particles are consistently smaller and exhibit higher dendricity compared to those on the surface, a trend explained by the force analysis showing that smaller and more branched particles possess a higher ratio of cohesive to gravitational forces (F_c/F_g), enhancing their attachment stability especially under edge conditions.

Based on the experimental result, the static force on the particle adhering to the edge has been analyzed. The model quantitatively explains the preferential adhesion of smaller and dendritic snow particles observed in experiments. The cohesion force model incorporates dendricity, reflecting the enhanced contact area and thus higher cohesion for non-spherical, dendritic particles compared to spherical ones. By introducing dendricity into the expression for cohesion force, the model can predict the threshold radius for particle adhesion as a function of dendricity, particle properties, and environmental parameters. The model highlights the critical role of particle shape and microstructure, alongside environmental conditions, in determining edge adhesion in snow cornices.

Although this study focuses on the initial stage of snow cornice formation at the micro-scale, the fundamental processes of adhesion of wind-transported snow particles are consistent across all scales, from laboratory conditions to natural environments. The direct experimental observations of single particles help bridge the gap between theoretical models and natural phenomena. Our experiments and findings enhance predictions of cornice growth and avalanche

risk, with broader implications for understanding snow adhesion on both natural features and infrastructure, such as ice crevasse formation and wire icing.

Future studies should continue to explore the interactions between environmental factors and particle behavior to refine our understanding of snow cornice dynamics. Numerical simulations will be essential for a more comprehensive understanding of the coupling between the flow field and snow cornice dynamics, and investigate the effects of mountain morphology on cornice growth.

Author contributions. YHX designed the experiments. YHX and LG carried out the experiments. YHX performed the data analysis, and prepared the first draft. ML, BW, HJP and HN reviewed and edited the paper. HN and ML organized this study, contributed to its conceptualization, discussion, and finalized the paper.

Competing interests. The authors declare that they have no conflict of interest.

Data availability. The data archiving is underway and will be added after it is published. Data is available on request.

Acknowledgements. The authors would like to thank the WSL Institute Snow and Avalanche Research SLF for making the experimental facilities available for our study. We thank Alec van Herwijnen for his invaluable experiment support. This work was supported by the Joint Funds of the National Natural Science Foundation of China (grant no.: U22A20564), the Young Scientists Fund of the National Natural Science Foundation of China (grant no.: 42406255), the Third Comprehensive Scientific Expedition and Research Program in Xinjiang (grant no.: 2022xjkk0101), China Postdoctoral Science Foundation (grant no.: 2024M751257), the Natural Science Foundation of Gansu Province (grant no.:24JRRA525) and the Swiss National Science Foundation (grant no.: 200020-179130). The data and code will be uploaded to the Dryad repository after the paper is published. Additionally, we are deeply grateful to the two anonymous reviewers and two scholars (Li Hongyi and Li Bailiang) for their insightful comments and constructive suggestions, which have greatly contributed to improving the quality and clarity of this paper.

References

Anderson, R. S. and Haff, P. K.: Wind modification and bed response during saltation of sand in air, in: Aeolian grain transport 1, pp. 21–51, Springer, 1991.

Baek, S. J. and Lee, S. J.: A new two-frame particle tracking algorithm using match probability, Experiments in Fluids, 22, https://doi.org/10.1007/BF01893303, 1996.

Bagnold, R. A.: The physics of blown sand and desert dunes, Courier Corporation, 2012.

Bartlett, S. J., Rüedi, J.-D., Craig, A., and Fierz, C.: Assessment of techniques for analyzing snow crystals in two dimensions, Annals of Glaciology, 48, 103–112, https://doi.org/10.3189/172756408784700752, 2008.

Colbeck, S. C.: An overview of seasonal snow metamorphism, Reviews of Geophysics, 20, 45–61, https://doi.org/https://doi.org/10.1029/RG020i001p00045, 1982.

Comola, F. and Lehning, M.: Energy- and momentum-conserving model of splash entrainment in sand and snow saltation, Geophysical Research Letters, 44, 1601–1609, https://doi.org/10.1002/2016GL071822, 2017.

Comola, F., Giometto, M., Salesky, S., Parlange, M., and Lehning, M.: Preferential Deposition of Snow and Dust Over Hills: Governing Processes and Relevant Scales, Journal of Geophysical Research: Atmospheres, 124, https://doi.org/10.1029/2018JD029614, 2019.

Crocker, J. C. and Grier, D. G.: Methods of Digital Video Microscopy for Colloidal Studies, Journal of Colloid and Interface Science, 179, 298–310, https://doi.org/https://doi.org/10.1006/jcis.1996.0217, 1996.

DeBonis, J.: A Large-Eddy Simulation Of Turbulent Flow Over A Backward Facing Step, https://doi.org/10.2514/6.2022-0337, 2022.

Di Stefano, L. and Bulgarelli, A.: A simple and efficient connected components labeling algorithm, in: Proceedings 10th International Conference on Image Analysis and Processing, pp. 322–327, https://doi.org/10.1109/ICIAP.1999.797615, 1999.

Eckerstorfer, M., Christiansen, H. H., Vogel, S., and Rubensdotter, L.: Snow cornice dynamics as a control on plateau edge erosion in central Svalbard, Earth Surface Processes and Landforms, 38, 466–476, 2013.

Golubev, V. N. and Frolov, A.: On the correlation between tensile strength and stress wave velocities of dry coherent snow based on its structural model, Annals of Glaciology, 32, 70–74, https://doi.org/10.3189/172756401781819562, 2001.

Gonzalez, R. C. and Woods, R. E.: Digital Image Processing 4th Edition, Pearson; 4th edition, 2017.

Hancock, H., Eckerstorfer, M., Prokop, A., and Hendrikx, J.: Quantifying seasonal cornice dynamics using a terrestrial laser scanner in Svalbard, Norway, Natural Hazards and Earth System Sciences, 20, 603–623, https://doi.org/10.5194/nhess-20-603-2020, 2020.

Jamieson, J. and Johnston, C.: In-Situ Tensile Tests of Snow-Pack Layers, Journal of Glaciology, 36, 102–106, https://doi.org/10.3189/S002214300000561X, 1990.

John, W.: Particle-Surface Interactions: Charge Transfer, Energy Loss, Resuspension, and Deagglomeration, Aerosol Science Technology, 23, 2–24, https://doi.org/10.1080/02786829508965291, 1995.

Latham, J. and Montagne, J.: The possible importance of electrical forces in the development of snow cornices, Journal of Glaciology, 9, 375–384, publisher: Cambridge University Press, 1970.

Loth, E.: Drag of non-spherical solid particles of regular and irregular shape, Powder Technology, 182, 342–353, https://doi.org/https://doi.org/10.1016/j.powtec.2007.06.001, 2008.

Lämmel, M., Dzikowski, K., Kroy, K., Oger, L., and Valance, A.: Grain-scale modeling and splash parametrization for aeolian sand transport, Physical Review E, 95, 022 902, https://doi.org/10.1103/PhysRevE.95.022902, 2017.

McClung, D. and Schaerer, P. A.: The avalanche handbook, The Mountaineers Books, 2006.

Montagne, J.: The University Course in Snow Dynamics—A Stepping-Stone to Career Interests in Avalanche Hazards, Journal of Glaciology, 26, 97–103, https://doi.org/10.3189/S0022143000010637, 1980.

Nishimura, K. and Hunt, J. C. R.: Saltation and incipient suspension above a flat particle bed below a turbulent boundary layer, Journal of Fluid Mechanics, 417, 77–102, https://doi.org/10.1017/S0022112000001014, 2000.

Paterna, E., Crivelli, P., and Lehning, M.: Decoupling of mass flux and turbulent wind fluctuations in drifting snow, Geophysical Research Letters, 43, 4441–4447, 2016.

Rafael, G. and Richard, W.: Digital Image Processing, in: Digital Image Processing, pp. 57–68, 1993.

Ren, Q., Ding, L., Dai, X., Jiang, Z., Ye, G., and De Schutter, G.: Determination of specific surface area of irregular aggregate by random sectioning and its comparison with conventional methods, Construction and Building Materials, 273, 122 019, 2021.

Schleef, S., Jaggi, M., Löwe, H., and Schneebeli, M.: An improved machine to produce nature-identical snow in the laboratory, Journal of Glaciology, 60, 94–102, https://doi.org/10.3189/2014JoG13J118, 2014.

Schmidt, R. A.: Threshold Wind-Speeds and Elastic Impact in Snow Transport, Journal of Glaciology, 26, 453–467, https://doi.org/10.3189/S0022143000010972, 1980.

Seligman, G., Seligman, G. A., and Douglas, C.: Snow structure and ski fields: being an account of snow and ice forms met with in nature, and a study on avalanches and snowcraft, Macmillan and Company, limited, 1936.

Shehadi, E.: Large Eddy Simulation of Turbulent Flow over a Backward-Facing Step, Ph.D. thesis, https://doi.org/10.13140/RG.2.2.17703.24480, 2018.

Solomon, C. J. and Breckon, T.: Fundamentals of Digital Image Processing: A Practical Approach with Examples in Matlab, 2011.

Sommer, C. G., Lehning, M., and Fierz, C.: Wind tunnel experiments: saltation is necessary for wind-packing, Journal of Glaciology, 63, 950–958, https://doi.org/10.1017/jog.2017.53, 2017.

Sommer, C. G., Lehning, M., and Fierz, C.: Wind tunnel experiments: influence of erosion and deposition on wind-packing of new snow, Frontiers in Earth Science, 6, 4, https://doi.org/10.3389/feart.2018.00004, 2018a.

Sommer, C. G., Wever, N., Fierz, C., and Lehning, M.: Investigation of a wind-packing event in Queen Maud Land, Antarctica, The Cryosphere, 12, 2923–2939, https://doi.org//10.5194/tc-12-2923-2018, 2018b.

Szabo, D. and Schneebeli, M.: Subsecond sintering of ice, Applied Physics Letters, 90, 151 916–151 916, https://doi.org/10.1063/1.2721391, 2007.

Tagliavini, G., Khan, M. H., Mccorquodale, M., Westbrook, C., and Holzner, M.: Wake characteristics of complex-shaped snow particles: Comparison of numerical simulations with fixed snowflakes to time-resolved particle tracking velocimetry experiments with free-falling analogs, Physics of Fluids, 34, 055 112, https://doi.org/10.1063/5.0089759, 2022.

van Herwijnen, A. and Fierz, C.: Monitoring snow cornice development using time-lapse photography, in: Proceedings of the International Snow Science Workshop, pp. 865–869, 2014.

Vogel, S., Eckerstorfer, M., and Christiansen, H. H.: Cornice dynamics and meteorological control at Gruvefjellet, Central Svalbard, The Cryosphere, 6, 157–171, https://doi.org/10.5194/tc-6-157-2012, 2012.

Wahl, S., Walter, B., Aemisegger, F., Bianchi, L., and Lehning, M.: Identifying airborne snow metamorphism with stable water isotopes, The Cryosphere, 18, 4493–4515, https://doi.org/10.5194/tc-18-4493-2024, 2024.

Walter, B., Weigel, H., Wahl, S., and Löwe, H.: Wind tunnel experiments to quantify the effect of aeolian snow transport on the surface snow microstructure, The Cryosphere Discussions, 2023, 1–27, https://doi.org/10.5194/tc-2023-112, 2023.

Walter, B., Weigel, H., Wahl, S., and Löwe, H.: Wind tunnel experiments to quantify the effect of aeolian snow transport on the surface snow microstructure, The Cryosphere, 18, 3633–3652, https://doi.org/10.5194/tc-18-3633-2024, 2024.

Yu, H., Li, G., Walter, B., Lehning, M., Zhang, J., and Huang, N.: Environmental Conditions for Snow Cornice Formation tested in a Wind Tunnel, The Cryosphere, pp. 1–15, https://doi.org/10.5194/tc-2022-27, 2022.